Universiteit
Leiden
The Netherlands

Transformation and sublimation of interstellar ices: insights from laboratory experiments and astronomical observations

Carvalho Santos, J. de

Citation

Carvalho Santos, J. de. (2025, July 2). *Transformation and sublimation of interstellar ices: insights from laboratory experiments and astronomical observations*. Retrieved from https://hdl.handle.net/1887/4252309

Version:	Publisher's Version
License:	Licence agreement concerning inclusion of doctoral thesis in the Institutional Repository of the University of Leiden
Downloaded from:	https://hdl.handle.net/1887/4252309

Note: To cite this publication please use the final published version (if applicable).

8. SO_2 and OCS toward high-mass protostars: a comparative study of ice and gas

OCS and SO_2 are both major carriers of gaseous sulfur and are the only sulfurated molecules detected in interstellar ices to date. They are thus the ideal candidates for exploring the evolution of the volatile sulfur content throughout the different stages of star formation. We aim to investigate the chemical history of interstellar OCS and SO_2 by deriving a statistically significant sample of gas-phase column densities toward massive protostars and comparing them to observations of gas and ices toward other sources, from dark clouds to comets. We analyzed a subset of 26 line-rich massive protostars observed by ALMA in Band 6 as part of the High Mass Protocluster Formation in the Galaxy (ALMAGAL) survey. Column densities were derived for OCS and SO_2 from their rare isotopologs $O^{13}CS$ and $^{34}SO_2$ toward the compact gas around the hot cores. We compared the abundance ratios of gaseous OCS, SO_2, and CH_3OH with ice detections toward both high- and low-mass sources as well as dark clouds and comets. We find that gas-phase column density ratios of OCS and SO_2 with respect to methanol remain fairly constant as a function of luminosity between low- and high-mass sources, despite their very different physical conditions. In our dataset, OCS and SO_2 are weakly correlated. The derived gaseous OCS and SO_2 abundances relative to CH_3OH are overall similar to protostellar ice values, with a significantly larger scatter for SO_2 than for OCS. Cometary and dark-cloud ice values agree well with protostellar gas-phase ratios for OCS, whereas higher abundances of SO_2 are generally seen in comets compared to the other sources. Gaseous SO_2/OCS ratios are consistent with ices toward dark clouds, protostars, and comets, albeit with some scatter. The constant gas-phase column density ratios throughout low- and high-mass sources indicate an early-stage formation before intense environmental differentiation begins. Icy protostellar values are similar to the gas-phase medians and are compatible with an icy origin for these species followed by thermal sublimation. The larger spread in SO_2 compared to OCS ratios with respect to CH_3OH is likely due to a more water-rich chemical environment associated with the former, as opposed to a CO-rich origin for the latter. Post-sublimation gas-phase processing of SO_2 can also contribute to the large spread. Comparisons to ices in dark clouds and comets point to a significant inheritance of OCS from earlier to later evolutionary stages.

J. C. Santos, M. L. van Gelder, P. Nazari, A. Ahmadi, E. F. van Dishoeck. 2024, Astronomy and Astrophysics, 689, A248.

8.1 Introduction

Over 240 molecules have been detected in the interstellar medium to date, among which at least 30 contain one or more sulfur atoms (McGuire 2022). With an abundance of S/H$\sim$1.35$\times$10^{-5}, sulfur is one of the most common elements in space (Asplund *et al.* 2009). S-bearing species are observed in the gas phase throughout most stages of star and planet formation, from diffuse and dense clouds (e.g., Drdla *et al.* 1989; Navarro-Almaida *et al.* 2020; Spezzano *et al.* 2022; Esplugues *et al.* 2022) and protostars (e.g., Blake *et al.* 1987, 1994; van der Tak *et al.* 2003; Li *et al.* 2015; Drozdovskaya *et al.* 2018; Codella *et al.* 2021; Artur de la Villarmois *et al.* 2023; Fontani *et al.* 2023; Kushwahaa *et al.* 2023) to protoplanetary disks (Fuente *et al.* 2010; Phuong *et al.* 2018; Semenov *et al.* 2018; Le Gal *et al.* 2019; Rivière-Marichalar *et al.* 2021; Le Gal *et al.* 2021; Booth *et al.* 2024). They have also been detected in Solar System bodies such as comets (Smith *et al.* 1980; Bockelée-Morvan *et al.* 2000a; Biver *et al.* 2021a,b; Calmonte *et al.* 2016; Altwegg *et al.* 2022), planets (Moullet *et al.* 2013), and satellites (Hibbitts *et al.* 2000; Jessup *et al.* 2007; Moullet *et al.* 2008; Cartwright *et al.* 2020), as well as toward extragalactic sources (Henkel & Bally 1985; Petuchowski & Bennett 1992; Mauersberger *et al.* 1995; Heikkilä *et al.* 1999; Martín *et al.* 2003, 2005). Identified species range from simple diatomic molecules such as CS and SO to the complex organics methanethiol and ethanethiol (CH_3SH and CH_3CH_2SH; Linke *et al.* 1979; Gibb *et al.* 2000; Cernicharo *et al.* 2012; Kolesniková *et al.* 2014; Zapata *et al.* 2015; Müller *et al.* 2016; Majumdar *et al.* 2016; Rodríguez-Almeida *et al.* 2021a).

Despite this widespread detection, derived abundances in dense starless cores, protostars, and protoplanetary disks can only account for up to a few percent of the total expected cosmic value (Tieftrunk *et al.* 1994; Wakelam *et al.* 2004; Anderson *et al.* 2013; Vastel *et al.* 2018; Fuente *et al.* 2019; Le Gal *et al.* 2019; Rivière-Marichalar *et al.* 2019, 2020; Le Gal *et al.* 2021; Bouscasse *et al.* 2022; Fuente *et al.* 2023). The bulk of the sulfur content is largely thought to be locked away in or underneath the ice mantles that shroud interstellar dust grains, in a state that makes its detection challenging. Such icy mantles start to form early in the interstellar evolutionary sequence, during the so-called translucent-cloud phase. Atoms of H and O adsorb onto dust grains and react to form H_2O, resulting in a water-rich ice layer (Tielens & Hagen 1982; Hiraoka *et al.* 1998; Mokrane *et al.* 2009; Dulieu *et al.* 2010; Ioppolo *et al.* 2010; Cuppen *et al.* 2010; Romanzin *et al.* 2011; Öberg *et al.* 2011a). As the density of the collapsing cloud increases, carbon monoxide (CO) molecules present in the gas phase catastrophically freeze out on top of the water-rich ice, forming a second coating known as the CO-rich ice layer (Tielens *et al.* 1991; Boogert *et al.* 2002; Pontoppidan *et al.* 2003; Pontoppidan 2006; Öberg *et al.* 2011a). This CO ice is efficiently converted into methanol (CH_3OH) by reactions involving H atoms (Tielens & Hagen 1982; Charnley *et al.* 1992; Hiraoka *et al.* 1994; Watanabe & Kouchi 2002; Fuchs *et al.* 2009; Cuppen *et al.* 2009; Santos *et al.* 2022b). Complementarily, some smaller contribution to CH_3OH formation from ice chemistry in less dense environments, before the catastrophic CO freeze-out, is also often invoked (e.g., Wada *et al.* 2006; Hodyss *et al.* 2009; Öberg *et al.* 2010b; Bergner *et al.* 2017; Lamberts *et al.* 2017; Qasim *et al.* 2018), although it is likely not dominant.

Eventually, the environment close to the emerging young stellar object is warmed up to temperatures of 100$-$300 K, resulting in the complete thermal sublimation of the ices. This chemically rich region surrounding the protostar is known as the hot core for massive sources or the hot corino for low-mass counterparts (e.g., Herbst & van Dishoeck 2009), and is thought to be representative of the bulk ice content. For simplicity, we henceforth utilize "hot core" as an umbrella term for both high- and low-mass sources. By studying the compact emission originated from the hot core in comparison to ice observations, it is possible to gain insight into the formation and destruction mechanisms of molecules in both the gas and solid phases.

Compared to gaseous species, the unambiguous detection of solid-state molecules embed-

ded in interstellar ices poses significantly more challenges. Spectral features of species in the solid phase are intrinsically broad and highly degenerate, with properties such as peak position and width that vary considerably with the ice environment. Likely as a consequence of such inherent limitations, only two sulfur-bearing species have been identified in ices so far: carbonyl sulfide (OCS) and sulfur dioxide (SO_2). The former was first detected by Palumbo *et al.* (1995) toward the massive protostar W33A. Soon after, Boogert *et al.* (1997) suggested the presence of the latter toward both W33A and NGC 7538:IRS1—another massive young stellar object (MYSO). Since then, both species have been either inferred or detected in ices toward other protostars as well as dark clouds (Palumbo *et al.* 1997; Öberg *et al.* 2008; Zasowski *et al.* 2009; Yang *et al.* 2022; Boogert *et al.* 2022; McClure *et al.* 2023; Rocha *et al.* 2024). Recently, the presence of SO_2 ice was confirmed by *James Webb* Space Telescope (JWST) observations toward the solar-type protostar IRAS 2A by constraining the contribution of blended species, in particular OCN^-, to its 7.6 μm region (Rocha *et al.* 2024).

In the gas phase, both species are commonly detected. Gaseous SO_2 is observed toward protostellar systems both through its pure rotational transitions occurring at submillimeter wavelengths and through its rovibrational lines probed by the mid-infrared (Keane *et al.* 2001; Dungee *et al.* 2018; Nickerson *et al.* 2023; van Gelder *et al.* 2024). It is a good tracer of outflows, jets, and accretion shocks due to its enhanced gas-phase formation at high temperatures ($T \gtrsim$100 K) combined with either sputtering or thermal sublimation of SO_2 or its precursors from icy dust grains (Pineau des Forêts *et al.* 1993; Sakai *et al.* 2014; Oya *et al.* 2019; Taquet *et al.* 2020; Tychoniec *et al.* 2021; van Gelder *et al.* 2021). It has also been shown to trace disk winds (Tabone *et al.* 2017). While this is the case for the main isotopolog (i.e., $^{32}SO_2$), the emission of minor isotopologs such as $^{34}SO_2$ is expected to be mostly compact, tracing the hot core region. Moreover, in contrast to SO_2, gaseous OCS emission is not expected to have significant contributions from outflows (van der Tak *et al.* 2003; Drozdovskaya *et al.* 2018), tracing predominately the envelope surrounding protostars (e.g., Herpin *et al.* 2009; Oya *et al.* 2016). As the only two sulfurated molecules detected in both gas and ices, SO_2 and OCS are the ideal targets for performing a comparative study between these two physical states.

In this work we explored the origin and fate of two of the most abundant sulfur species, OCS and SO_2, by directly comparing their solid and gaseous components during the evolution of star-forming regions. We utilized data from the ALMA Evolutionary study of High Mass Protocluster Formation in the Galaxy (ALMAGAL) survey and selected a subsample of 26 line-rich sources to perform the analysis. This is the first interferometric study on a statistically significant sample of detections for these two molecules in the gas phase. The molecular column densities were derived from the rare isotopologs $O^{13}CS$ and $^{34}SO_2$ to avoid contamination from extended emission and to limit line optical depth effects. We thus focused on the hot core region, which contains the molecular reservoir from the ices after complete thermal sublimation. We compared their ratios to other observations in the solid and gas phases taken from the literature. This includes recent work that utilized ground-based infrared observatories to investigate OCS ice abundances (among other species) in a large sample of MYSOs (Boogert *et al.* 2022), as well as space observations by JWST of both OCS and SO_2 ices toward sources ranging from background stars to protostars (McClure *et al.* 2023; Rocha *et al.* 2024). This work sets the stage for future studies of gas and ice enabled by the combination of data from the Atacama Large Millimeter/submillimeter Array (ALMA) and JWST on both low- and high-mass protostars, paving the way to a more thorough understanding of the sulfur chemical evolution of the interstellar medium.

In Sect. 8.2 we describe the observational parameters and details of the dataset, as well as the procedure for fitting a synthetic spectrum to the lines of interest. The resulting emission morphologies, kinematics, and column densities are presented in Sect. 8.3. The column density ratios with respect to methanol and in comparison to other observations are discussed in Sect. 8.4. Finally, our main findings and conclusions are summarized in Sect. 8.5.

8.2 Observations and methods

8.2.1 The observations

The ALMAGAL survey (2019.1.00195.L; PIs: P. Schilke, S. Molinari, C. Battersby, P. Ho) was observed by ALMA in Band 6 (∼1 mm). It targeted over 1000 dense clumps across the Galaxy with $M > 500$ $M_\odot$ and $d < 7.5$ kpc, chosen based on the Herschel infrared Galactic Plane Survey (Hi-GAL; Molinari *et al.* 2010; Elia *et al.* 2017, 2021). ALMAGAL covers a statistically significant sample of sources in all stages of star formation, with many of them consisting of MYSOs. For this work we considered only archival data made publicly available before February 2021 and with beam sizes between 0.5″and 1.5″(∼1000–5000 au). The Common Astronomy Software Applications[1] (CASA; McMullin *et al.* 2007) version 5.6.1. was used to pipeline calibrate and image the data. The selection of sources was based on a subset studied in both Nazari *et al.* (2022) and van Gelder *et al.* (2022a), thus culling for particularly line-rich sources for which the CH_3OH column densities—our benchmark for comparison—are well constrained. In van Gelder *et al.* (2022a), the selection was based on sources with high bolometric luminosities ($L_{\rm bol} > 1000$ $L_\odot$) where complex organic molecules such as CH_3OH and CH_3CN were detected. In Nazari *et al.* (2022), the selection criterium consisted of sources that contain the CH_3CN 12_7–11_7 line above the 2.5−3σ level. Within the subset studied by both Nazari *et al.* (2022) and van Gelder *et al.* (2022a), we excluded sources for which the line profiles of the targeted molecules differed significantly across species, to avoid probing distinct emitting regions. An example case of an excluded source is shown in Appendix 8.7.1. The final subset consists of 26 line-rich sources, whose properties and observational parameters are listed in Appendix 8.7.2.

In this work we made use of two out of the four spectral windows in ALMAGAL, encompassing frequencies of ∼217.00−218.87 GHz and ∼219.07−220.95 GHz with a spectral resolution of ∼0.5 MHz (∼0.7 km s^{-1}). The spectral windows cover 4 transitions of $^{34}SO_2$, 11 transitions of $^{33}SO_2$, and 1 transition of $O^{13}CS$ with upper energy $E_{\rm up} < 800$ K and Einstein $A_{\rm ij} > 1 \times 10^{-6}$ s^{-1} (see Appendix 8.7.3). However, only the $11_{1,11}$–$10_{0,10}$ transitions of $^{34}SO_2$ and $^{33}SO_2$ were detected in our sources ($E_{\rm up}$ = 60.1 K and 57.9 K, respectively). For $^{34}SO_2$, this corresponds to only one line, whereas for $^{33}SO_2$ it encompasses 7 hyperfine components caused by the nuclear spin $I = 3/2$ of the ^{33}S atom. The remaining $^{34}SO_2$ and $^{33}SO_2$ lines are rather weak ($A_{ij} < 2.6 \times 10^{-5}$ s^{-1}) and for the most part highly blended, hampering their detections. $O^{13}CS$ is detected in its 18−17 transition ($E_{\rm up}$ = 99.5 K). No other isotopologs of OCS, including $O^{12}CS$, are covered in the ALMAGAL range. One line of $^{32}SO_2$ is covered, but it is not included in this work due to its likely contamination from outflow emission and because it is probably optically thick.

The spectra utilized in this work are the same as in van Gelder *et al.* (2022a). For all sources with the CH_3OH $8_{0,8}$–$7_{1,6}$ line ($E_{\rm up}$ = 97 K) above the 3σ level, the spectra were extracted from the peak pixel for this line in the integrated intensity maps. This particular transition of CH_3OH was chosen because it is the strongest methanol line within the sample with $E_{\rm up} > 70$ K, to avoid contamination by the outflow or extended emission that are probed by lines with lower $E_{\rm up}$. The choice of extracting the spectra from the methanol peak intends to maximize the signal-to-noise ratio of both $^{34}SO_2$ and $O^{13}CS$ originating from the hot core region. In G023.3891p00.1851, the peak emission of the methanol isotopolog CH_2DOH is offset by $\sim 0.6''$ (approximately half a beam) from that of CH_3OH, and thus the CH_2DOH $17_{1,16}e_0$–$17_{0,17}e_0$ ($E_{\rm up}$ = 336 K) peak is chosen to extract the spectrum since it is a more reliable tracer of the hot core. All sources probed here show line widths of $\gtrsim 3$ km s^{-1}, well above the spectral resolution of ~ 0.7 km s^{-1}, and the spectral sensitivity corresponds to ~ 0.2 K (for a list of rms values see Appendix 8.7.2).

[1] https://casa.nrao.edu

8.2.2 Spectral analysis

The target molecules of this study are SO_2 and OCS, the two sulfur-bearing species detected in both gas and ices so far. We analyzed them by means of their rare isotopologs $^{34}SO_2$ and $O^{13}CS$ in order to avoid issues with optically thick lines and contamination from extended emission and outflows. The $^{33}SO_2$ emission is also analyzed as a diagnostic tool to assess whether or not $^{34}SO_2$ is indeed optically thin (Sect. 8.3.3). We utilized the CASSIS[2] spectral analysis tool (Vastel *et al.* 2015) to fit the spectrum for each source and derive each species' column density (N) and full width at half maximum (FWHM) assuming that the excitation is under local thermodynamic equilibrium. Since we only detect one line per species per source, the excitation temperature was fixed to $T_{\rm ex}$ = 150 K in the spectral fittings—a roughly averaged value for hot cores (see, e.g., van Gelder *et al.* 2020; Yang *et al.* 2021; Nazari *et al.* 2022). Fixing the $T_{\rm ex}$ to 60−250 K only changes the derived column densities by up to a factor of $\sim$ 3, and both molecules in the same direction. Furthermore, for $\gtrsim$ 80% of the sources in this work, excitation temperatures derived from CH_3CN lines range between 120 and 170 K (Nazari *et al.* 2022), corresponding to only up to a factor of 1.6 difference in column densities for SO_2 and OCS. Thus, the assumption of a fixed $T_{\rm ex}$ = 150 K does not interfere significantly with the column density ratios—the main focus of this work. The spectroscopic properties employed in the fittings of each species are obtained from the Cologne Database for Molecular Spectroscopy (CDMS; Müller *et al.* 2001, 2005).

The $^{34}SO_2$ and $O^{13}CS$ lines analyzed in this work are mostly unblended, which allows the utilization of the grid fitting method as explained in detail previously (van Gelder *et al.* 2020; Nazari *et al.* 2021; Chen *et al.* 2023). In summary, a grid of column densities and FWHMs is tested and the best-fit model is assigned to the combination with the lowest χ^2. In this work N was varied from 1×10^{13} cm^{-2} to 1×10^{17} cm^{-2} with a step of 0.1 on a logarithmic scale, and the FWHM was varied from 3 km s^{-1} to 11 km s^{-1} with a spacing of 0.1 km s^{-1} on a linear scale. The radial velocities ($V_{\rm lsr}$) are derived by eye using increments of 0.1 km s^{-1} in a similar manner as described in Nazari *et al.* (2022) and Chen *et al.* (2023), and are fixed to the best manually derived values for the grid fits. Their median offsets are of 0.35 km s^{-1} from the velocities for CH_3OH in the same sources (see Sect. 8.3.2). The 2σ errors are derived from the reduced χ^2 calculated from the comparison between the resulting model of each grid point and the observed spectrum. If the 2σ uncertainties of the column densities are smaller than 20%, we assumed a 20% uncertainty as a conservative estimate to account for systematic sources of errors. In a few instances, such as for $^{34}SO_2$ in 693050, more severe blending or deviations from a Gaussian profile are observed (see Appendix 8.7.4). Nonetheless, the integrated line emissions are still encompassed by our models well within the adopted conservative uncertainties, and thus it does not affect our analysis. In the cases of G025.6498p01.0491 for $^{34}SO_2$, and 126348 and 707948 for $O^{13}CS$, the emission is better described by two components (see Appendix 8.7.4). However, obtaining column density ratios for each velocity component separately is not possible since they are not resolved for methanol. In such cases, we performed the grid fits assuming one Gaussian and fixing the $V_{\rm lsr}$ to the mean between the values derived by eye for each component. This procedure yields column densities within 20% of the ones obtained by manually fitting each component separately. Thus, to ensure a systematic approach to the line analysis, we utilized the column densities derived from the grid fittings to these sources. The exact source sizes are not known, so we assumed that the source fully fills the beam (i.e., a beam dilution factor of unity). Since this work focuses on comparing column density ratios, this assumption does not interfere with the analysis as long as the lines are optically thin (van Gelder *et al.* 2020; Nazari *et al.* 2021).

Fitting $^{33}SO_2$ is more challenging. It is considerably less abundant than $^{34}SO_2$, and its only detected transitions are blended with $CH_3{}^{13}CN$. The fitting was thus performed by eye on top of the best models for $CH_3{}^{13}CN$ derived by Nazari *et al.* (2022). The $V_{\rm lsr}$ values of $^{33}SO_2$ were fixed to those of $^{34}SO_2$, while its column densities and FWHMs were varied in

[2]http://cassis.irap.omp.eu/

steps of 0.1 in log space and 0.1 in linear space, respectively. For most sources, barely or no emission was left underfit after accounting for $CH_3{}^{13}CN$. In such cases we assigned $^{33}SO_2$ as upper limits. However, for four sources (615590, 644284A, 693050, and G343.1261-00.0623) the $CH_3{}^{13}CN$ model underfit the emission significantly ($\lesssim$50%), in which cases we could derive approximate column densities for $^{33}SO_2$.

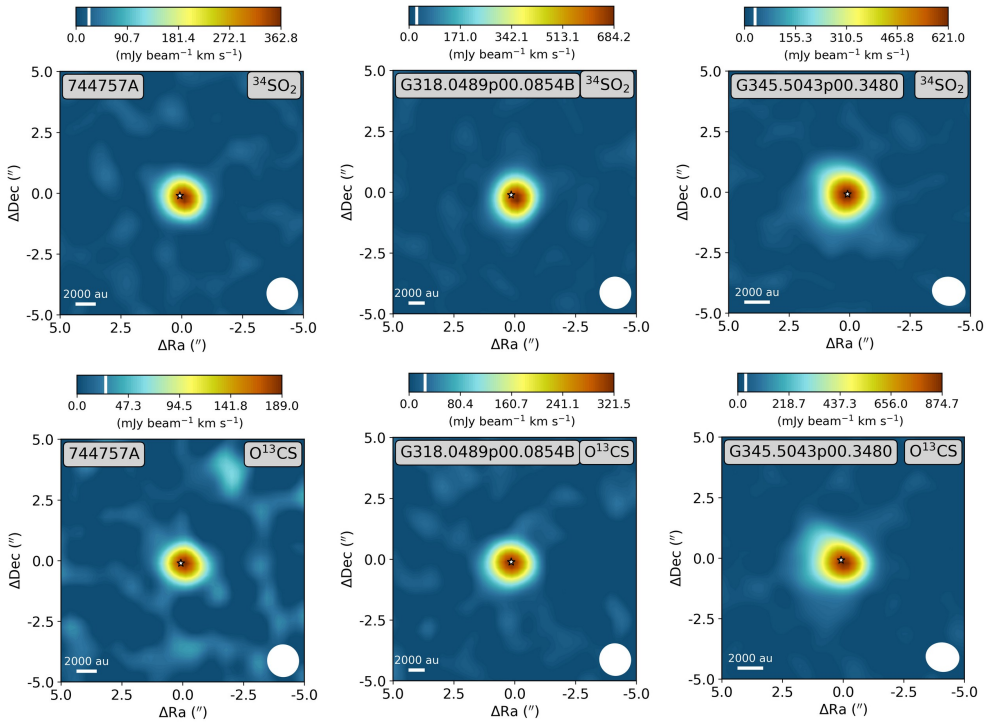

Figure 8.1: Integrated intensity maps of the $^{34}SO_2$ $11_{1,11}$–$10_{0,10}$ (E_{up} = 60.1 K, top) and $O^{13}CS$ 18−17 (E_{up} = 99.5 K, bottom) lines for 744757A, G318.0489p00.0854B, and G345.5043p00.3480. The integration limits are set to [-2, 2] km s^{-1} with respect to the sources' V_{lsr}. The white star denotes the source positions derived from the peak continuum emission, and the 3σ threshold is denoted by the white line in the color bars. The beam size is shown in the lower-right corner of each panel, and a scale bar is depicted in the lower left.

8.2.3 Isotope ratio calibration

Isotopic abundances are dependent on the stellar population and therefore vary as a function of the distance to the Galactic center (D_{GC}). In order to obtain accurate column densities of the main SO_2 and OCS isotopologs, it is thus required to calibrate the isotope ratios of ($^{32}S/^{34}S$), ($^{32}S/^{33}S$), and ($^{12}C/^{13}C$) accordingly. Recently, Yan *et al.* (2023) utilized CS lines in a wide variety of isotopologs observed toward 110 high-mass star-forming regions to derive the equations

$$(^{32}S/^{34}S) = (0.73 \pm 0.36) D_{GC} + (16.50 \pm 2.07), \tag{8.1}$$

$$(^{32}S/^{33}S) = (2.64 \pm 0.77) D_{GC} + (70.80 \pm 5.57), \tag{8.2}$$

$$(^{12}C/^{13}C) = (4.77 \pm 0.81) D_{GC} + (20.76 \pm 4.61). \tag{8.3}$$

The D_{GC} can be calculated based on the source's distance to Earth (d) and its coordinates. The resulting values for each source are listed in Appendix 8.7.2 and are used to derive $^{32}SO_2$ and $O^{12}CS$ from the isotopologs. For the solar neighborhood, the ratios are ($^{32}S/^{34}S$)$\sim$22, ($^{32}S/^{33}S$)$\sim$92, and ($^{12}C/^{13}C$)$\sim$59. The uncertainties in the final column densities of $^{32}SO_2$ and $O^{12}CS$ (henceforth simply SO_2 and OCS) are obtained by propagating the errors in the derived column densities of the minor isotopologs together with the uncertainties in Eqs. 8.1−8.3 and the typical error of $\sim$0.5 kpc in D_{GC} (see Nazari *et al.* 2022).

8.3 Results

8.3.1 Morphology

The integrated intensity maps of $^{34}SO_2$ and $O^{13}CS$ for 744757A, G318.0489p00.0854B, and G345.5043p00.3480 are presented in Fig. 8.1. These are chosen as a representative sample of the sources analyzed in this work. The emission areas of both species are compact (with typical radii of $\sim$1000−3000 au considering all sources) and mostly unresolved, in accordance with the expectation that rare isotopologs likely trace the hot core region with little to no contribution from extended emission. The case of 693050 is an exception in which the $^{34}SO_2$ and $O^{13}CS$ peaks are offset from the continuum peak (as shown by the white star) by $\sim$4000 au (see Appendix 8.7.5). This could be the result of optically thick dust at these wavelengths, leading to continuum over-substraction or dust attenuation toward the continuum peak, which has been shown to hide molecular emission in protostellar systems (De Simone *et al.* 2020). Indeed, the same behavior is observed for CH_3OH emission in 693050, in line with this hypothesis (van Gelder *et al.* 2022b). Higher spatial resolution is required to fully distinguish the species' emitting regions. Still, some spatial information can be acquired by comparing their best-fit parameters (see Sect. 8.3.2).

8.3.2 Fitting results

The best-fit parameters of $^{34}SO_2$ and $O^{13}CS$ for all sources are listed in Appendix 8.7.6, together with the corresponding column densities derived for SO_2 and OCS. The best-fit models are shown in Fig. 8.2 for a set of representative sources: 744757A, G318.0489p00.0854B, and G345.5043p00.3480. The models for the remaining sources are presented in Appendix 8.7.4. 3σ upper limits are provided when line intensities do not surpass this detection threshold. For most sources, the $^{34}SO_2$ column densities range between 10^{15} and 10^{16} cm^{-2}, which corresponds to SO_2 column densities of 10^{16}–10^{17} cm^{-2}. The only exceptions to this trend are the sources for which only $N(^{34}SO_2)$ upper limits could be derived.

In comparison, the $O^{13}CS$ column densities are roughly one order of magnitude lower, but given the larger ratios of ($^{12}C/^{13}C$) compared to ($^{32}S/^{34}S$), the corresponding N(OCS) values also range between 10^{16} and 10^{17} cm^{-2}. Absolute column densities are nevertheless subject to biases such as the assumed emitting area and thus are not ideal to be directly compared. Column density ratios are a more reliable form of comparison to provide information on the chemical inventories of different systems. The column densities derived in this work will be discussed in detail in Sect. 8.4.

Despite the emissions probed here being largely unresolved, line widths and velocities can be utilized to infer the kinematics of the gas. In Appendix 8.7.7, we present a comparison between the widths and velocities for both $^{34}SO_2$ and $O^{13}CS$ with respect to $CH_3{}^{18}OH$. The latter were obtained from the fittings performed by van Gelder *et al.* (2022a). For some sources, van Gelder *et al.* (2022a) did not detect $CH_3{}^{18}OH$, in which cases we compared them to the fitting parameters of the main CH_3OH isotopolog (signaled by empty markers). The median offsets of the line widths and peak velocities between the three different species are,

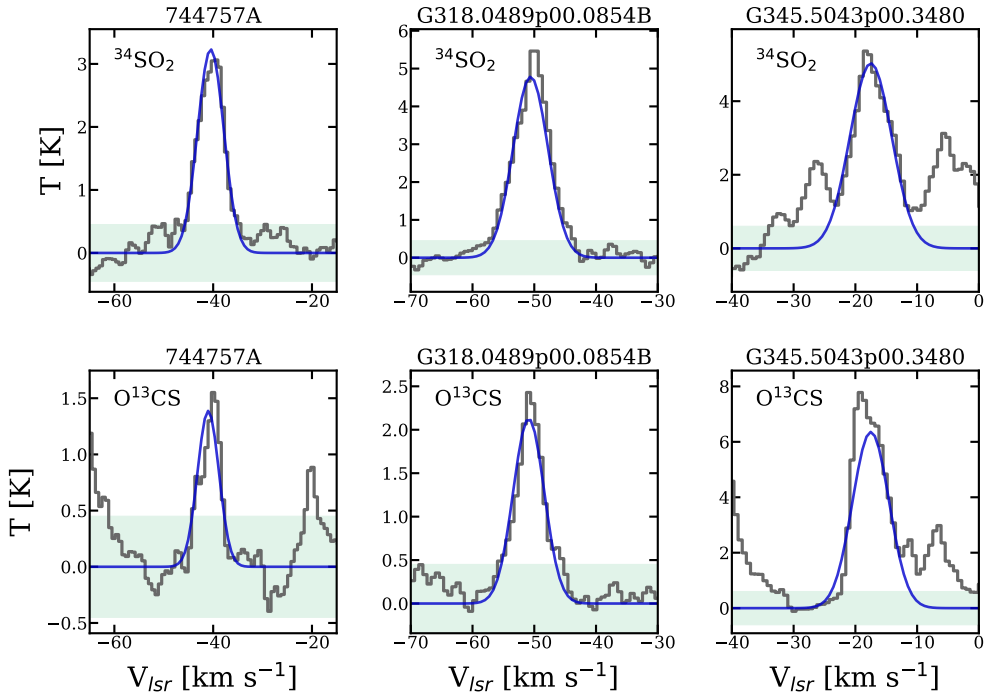

Figure 8.2: Observed spectra toward 744757A, G318.0489p00.0854B, and G345.5043p00.3480 (gray) superimposed by their best-fit models (blue). The upper panels show the lines of $^{34}SO_2$ ($11_{1,11}$–$10_{0,10}$), and the lower panels lines of $O^{13}CS$ (18–17). The green shadowed area delimits the 3σ threshold.

respectively, 0.15 and 0.35 km s^{-1}. This is in line with all three molecules tracing a similar compact gas within the hot core region and serves as validation for a comparative analysis of their column density ratios. The fact that no distinctively large discrepancy in FWHM and $V_{\rm lsr}$ is observed for $^{34}SO_2$ is an indication that any contribution from outflows to this line can be neglected.

8.3.3 Is $^{34}SO_2$ optically thin?

Line emissions from rare isotopologs are usually assumed to be optically thin. However, this is not necessarily always true, especially for abundant species such as SO_2. For this reason, we utilized the four sources in which $^{33}SO_2$ is detected to assess whether $^{34}SO_2$ is indeed optically thin. Their best-fit parameters are listed in Appendix 8.7.8. We derived the column densities of SO_2 (i.e., of the main isotopolog) from both $N(^{34}SO_2)$ and $N(^{33}SO_2)$ separately, using their isotope ratios as described in Sect. 8.2.3. Figure 8.3 shows the ratios of SO_2 column densities derived from $^{34}SO_2$ over the $^{33}SO_2$ counterparts for the four sources. The resulting values are all remarkably close to unity, confirming that both the $^{34}SO_2$ and $^{33}SO_2$ lines are indeed optically thin. In fact, the larger the $N(SO_2)/N(CH_3CN)$ ratios (indicated by the red arrow), the closer the values are to unity. Given that the $^{33}SO_2$ lines had to be fitted on top of $CH_3{}^{13}CN$ (see the discussion in Sect. 8.2.2), this strongly suggests that the small discrepancies in SO_2 column densities calculated from $N(^{33}SO_2)$ and $N(^{34}SO_2)$ are mostly due to $^{33}SO_2$ being heavily blended.

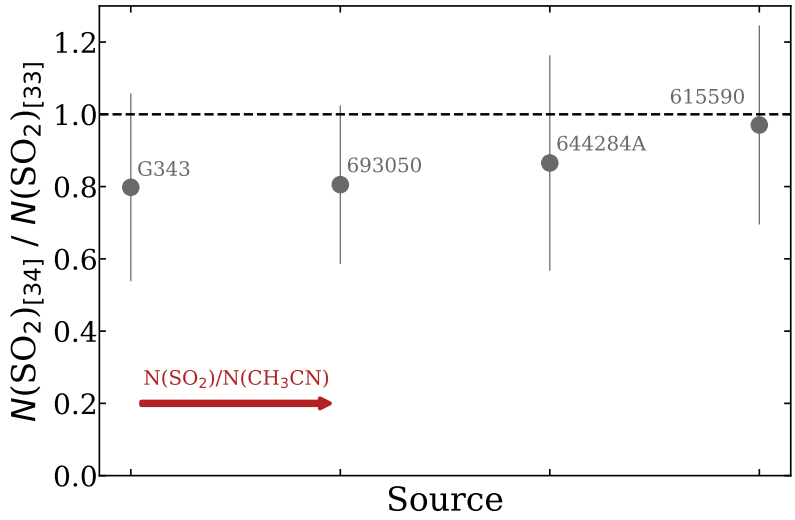

Figure 8.3: Ratios of $N(^{32}SO_2)$ derived from $N(^{34}SO_2)$ (numerator) over those derived from $N(^{33}SO_2)$ (denominator). The red arrow indicates that the sources are sorted in order of increasing $N(SO_2)/N(CH_3CN)$ relative abundances. The dashed line highlights the unity mark. G343 stands for source G343.1261-00.0623.

8.4 Discussion

As mentioned in Sect. 8.3.2, column density ratios are a good metric to compare the chemical content of different sources and types of environments. Here we utilized the CH_3OH column densities derived by van Gelder *et al.* (2022a) from minor isotopologs as a basis for comparison. Given the ice origin of methanol, it is possible to deduct information on the chemical history of OCS and SO_2 from their relative abundances with respect to CH_3OH. In the following subsections, we compare $N(OCS)/N(CH_3OH)$ and $N(SO_2)/N(CH_3OH)$ derived in this work with relative abundances taken from the literature. These encompass gas-phase observations toward both MYSOs and low-mass young stellar objects (LYSOs), ice observations toward protostars and dark clouds, as well as cometary ratios. A complete list of references from which these ratios are taken can be found in Appendix 8.7.9.

8.4.1 $N(OCS)/N(CH_3OH)$

Figure 8.4 shows a comparison of the column density ratios of $N(OCS)/N(CH_3OH)$ for various objects. It includes gas-phase observations in low- and high-mass sources as well as ice observations in MYSOs, in dark clouds, and in comets (see Appendix 8.7.9 for a list of references). The ratios derived in this work are shown in blue. In general, no trend in ratio versus luminosity is observed. Indeed, the data points for protostars (including both ice and gas phases) result in a Pearson correlation coefficient (r) of only -0.11. Spearman correlation tests are also performed and yield similar results to Pearson's for all cases explored in this work. Figure 8.4 also contain single-dish observations, but since these probe a much larger scale compared to interferometric counterparts, they are not included in the analysis. Furthermore, Kushwahaa *et al.* (2023) note that their observations could be subject to beam dilution, which could affect the gas-phase ratios for most of the low-mass sources shown in Fig. 8.4 (with the exception of IRAS 16293-2422 B). Nonetheless, they can still provide information on general trends in abundances. The fairly constant abundance ratios observed

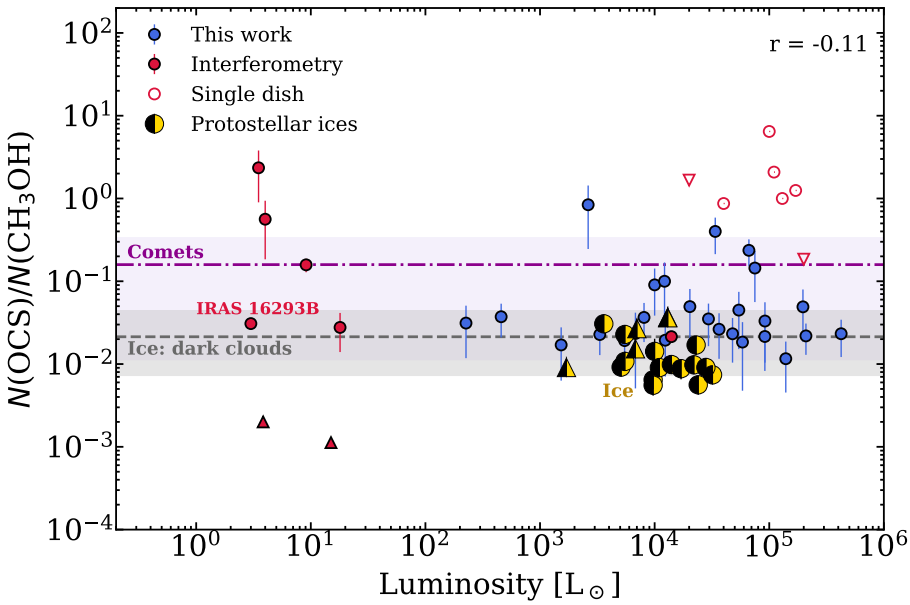

Figure 8.4: Column density ratios $N(\mathrm{OCS})/N(\mathrm{CH_3OH})$ derived in this work (blue markers) for 26 high-mass protostars as a function of luminosity. Literature gas-phase values are shown for comparison (red markers), together with ice values in protostars (yellow and black markers), dark clouds (gray dashed line), and comets (purple dash-dot line). The references can be found in Appendix 8.7.9. Upper and lower limits towards protostars are denoted by downward- and upward-facing triangles, respectively. The range of values for dark clouds and comets are shown by their respective shadowed areas. For gas-phase ratios, filled markers correspond to interferometric observations, whereas empty markers denote single dish counterparts. The Pearson correlation coefficient for protostellar ratios in both gas and ices, but excluding single-dish observations and lower limits, is displayed in the upper right corner. IRAS 16293B stands for the source IRAS 16293-2422 B.

throughout all sources indicate that OCS must be formed under similar conditions irrespective of the mass (or luminosity) of the protostar. Considering the drastically different physical conditions experienced by MYSOs and LYSOs during their evolution, particularly regarding their temperatures and UV fields, this lack of correlation with respect to luminosity points to an early formation of the bulk of OCS under cold and dense conditions, prior to the onset of star formation. More data points for low-mass sources would be useful to further constrain any potential trend obscured by the scatter in the ratios.

A considerable number of data points are available for $N(\mathrm{OCS})/N(\mathrm{CH_3OH})$ ratios in protostellar ices (Boogert *et al.* 2022), which enables a statistically significant analysis. Using abundance distribution histograms is an instructive approach to comparing different, large datasets (see, e.g., Öberg *et al.* 2011a). In Fig. 8.5, the log-transformed $N(\mathrm{OCS})/N(\mathrm{CH_3OH})$ ratios are presented for both ice and gas observations toward MYSOs, and are centered on the weighted median of the ALMAGAL dataset ($\sim$0.033). Ice lower limits affect the median value by $< 5\%$ and are thus not included in the analysis. Overall, the ice ratios in MYSOs are slightly lower than the gas-phase counterparts, with a difference of a factor of $\sim$3 between their weighted medians. This discrepancy is remarkably small, and could be due to the

uncertainties in the spectral analysis (especially considering the approximation of a fixed $T_{\rm ex}$). Such strikingly similar ratios provide strong evidence of an icy origin for OCS.

Furthermore, both ice and gas datasets have small scatters, which suggests that the column densities of CH_3OH and OCS are subject to similar dependences. A spread factor f, defined by 10 to the power of the weighted 1σ standard deviation measured in log10 space, serves as a convenient comparison basis between distinct datasets (see, e.g., Nazari *et al.* 2023). Table 8.1 summarizes the weighted median gas-phase ratios and spread factors derived in this work for $N(\rm OCS)/N(CH_3OH)$, $N(\rm SO_2)/N(CH_3OH)$, and $N(\rm SO_2)/N(OCS)$. For the ALMAGAL subset, the $N(\rm OCS)/N(CH_3OH)$ ratios results in $f = 2.8$, whereas ice observations in MYSOs have $f = 1.9$. These small scatters suggest similar conditions during the formation of the bulk of OCS and CH_3OH, strengthening the conclusion of an icy origin to OCS followed by thermal sublimation. It is worth noting that the lower limits in the available ice ratios are either equivalent to or higher than the corresponding weighted median, so a high abundance tail similar to the gas-phase case could be plausible.

Table 8.1: Weighted medians of the column density ratios and spread factors derived in this work for gas-phase species in massive sources (not including upper limits).

Ratio	Weighted median	Spread factor
$N(\rm OCS)/N(CH_3OH)$	0.033	2.8
$N(\rm SO_2)/N(CH_3OH)$	0.044	5.8
$N(\rm SO_2)/N(OCS)$	1.103	3.7

The small scatter for OCS points to an ice environment similar to CH_3OH. This agrees with the main proposed chemical routes to form OCS, which involve the sulfurization of CO ices. Laboratory experiments show that OCS ice can be readily formed by the reactions (Ferrante *et al.* 2008; Jiménez-Escobar *et al.* 2014a; Chen *et al.* 2015; Nguyen *et al.* 2021b; Santos *et al.* 2024b)

$$\rm s{-}CO + s{-}S \rightarrow s{-}OCS \tag{8.4}$$

$$\rm s{-}CO + s{-}HS \rightarrow s{-}OCS + s{-}H, \tag{8.5}$$

which can either be induced by thermalized S and SH adsorbed on the ice or as a result of the energetic processing of larger species (e.g., CO_2 and H_2S). Indeed, Boogert *et al.* (2022) analyzed a large sample of ice observations toward massive protostars and conclude that OCS and CH_3OH column densities are correlated, pointing to an OCS formation concomitant with CH_3OH during the dense pre-stellar core stage, with both sharing CO as a common precursor.

Comparisons with dark clouds prior to star formation and comets are also relevant to constrain the evolution of sulfur species in both solid and gas phases. Observed $N(\rm OCS)/N(CH_3OH)$ ice ratios in dark clouds agree strikingly well with the protostellar observations toward both ice and gas. This is in full support of the hypothesis that OCS is formed in the ices within pre-stellar cores. Caution should be taken when comparing these values, however, since only two data points are available for ices in pre-stellar cores so far (McClure *et al.* 2023). Nonetheless, it can still provide the basis for an interesting preliminary comparison. Cometary ratios, in turn, are marginally higher (by a factor of $\sim$4) than the weighted median for ALMAGAL, although their spread encompasses both gas and ice observations. This small discrepancy could be due to additional processing of OCS during the protostellar disk phase (as was also suggested by Boogert *et al.* 2022) or as a result of selective CH_3OH destruction before incorporation into comets. The latter has been previously suggested by Öberg *et al.* (2011a) as one explanation to the depletion of cometary CH_3OH, CH_4, and CO ices relative

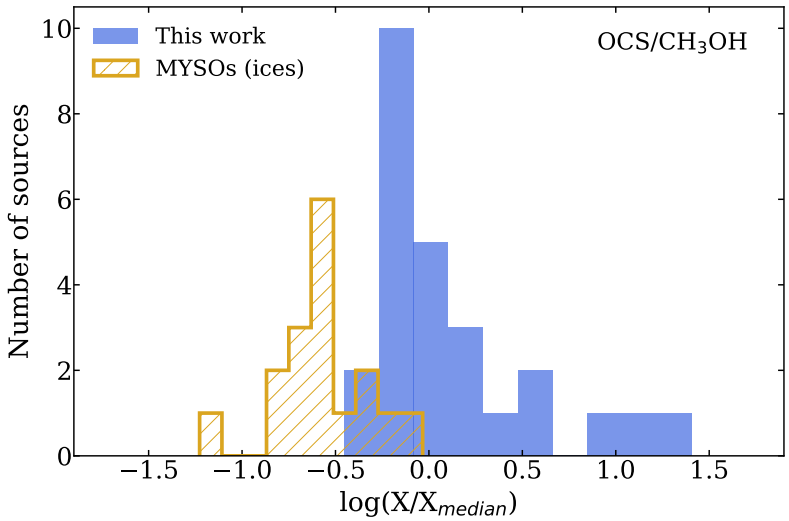

Figure 8.5: Relative abundance distributions of $N(\mathrm{OCS})/N(\mathrm{CH_3OH})$ for the gas-phase observations of massive sources analyzed in this work (blue) compared to ice observations toward 20 MYSOs by (Boogert *et al.* 2022, yellow). Both histograms are normalized to the weighted gas-phase median value derived from the ALMAGAL dataset for 26 high-mass protostars.

to H_2O compared to protostars. However, given that OCS and CH_3OH are mixed, it seems unlikely that a destruction mechanism could affect one but not the other.

8.4.2 $N(\mathrm{SO_2})/N(\mathrm{CH_3OH})$

Figure 8.6 shows a comparison of the column density ratios of $N(\mathrm{SO_2})/N(\mathrm{CH_3OH})$. Similarly to OCS, no correlation is observed for the column density ratios in protostars as a function of luminosity (Pearson $r = -0.08$), in support of the hypothesis of an early formation during the pre-stellar core stage. One caveat to this conclusion is that the gaseous SO_2 column densities in LYSOs are derived from its major isotopolog for most sources (light-red points in Fig. 8.6), which could contain appreciable contamination from outflow emission and could be optically thick. In fact, Artur de la Villarmois *et al.* (2023) estimate that ∼40% of the SO_2 emission in their study is extended. The only exception among low-mass sources is the data point corresponding to IRAS 16293–2422 B, for which SO_2 column densities are derived from $^{34}SO_2$ (dark-red point in Fig. 8.6). Further works focused on compact, optically thin SO_2 emission (as traced by, e.g., $^{34}SO_2$) in low-mass sources are warranted to further evaluate this hypothesis.

In contrast to OCS, ice ratios of $N(\mathrm{SO_2})/N(\mathrm{CH_3OH})$ in protostars are still scarce. However, the available values so far for both high-mass and low-mass sources taken from Boogert *et al.* (1997, 2022) and Rocha *et al.* (2024) agree fairly well with the median gas-phase ratios derived in this study. The weighted median for our subset of MYSOs (excluding upper limits) is ~ 0.044, which is consistent with both ice ratios of 0.06 ± 0.04 and 0.07 ± 0.04 in a low- and high-mass source, respectively. This agrees with the hypothesis that SO_2 is primarily formed in ices prior to the onset of star formation, and later sublimates upon thermal heating by the protostar.

The scatter in the ALMAGAL values is considerably larger than that for OCS, which suggests that the column densities of CH_3OH and SO_2 are subject to different dependences.

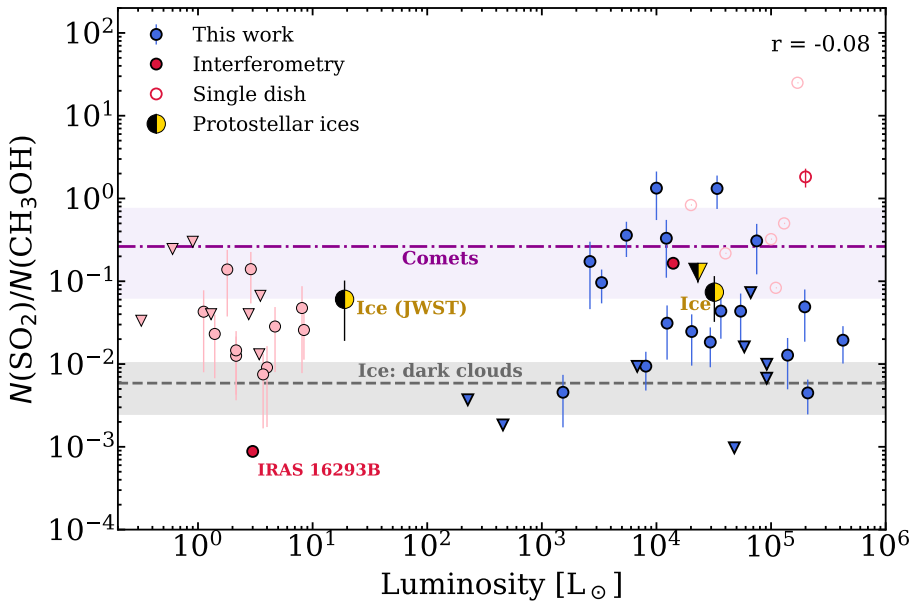

Figure 8.6: Same as Figure 8.4, but for $N(SO_2)/N(CH_3OH)$. Literature ratios with $N(SO_2)$ derived from the main isotopologue are signaled by light red markers to differentiate from values derived from $^{34}SO_2$, which are shown in darker red. The data point for the low-mass protostellar ice ratio corresponds to the JWST observations towards IRAS 2A (Rocha *et al.* 2024), and the high-mass ice ratios correspond to airborne (KAO) and ground-base (IRTF) observations towards W33A and NGC 7538 IRS 9 (upper limit) (Boogert *et al.* 1997, 2022).

For the ALMAGAL subset, $N(SO_2)/N(CH_3OH)$ ratios result in $f = 5.8$. For comparison, oxygen and nitrogen-bearing complex organic molecules typically have $N(X)/N(CH_3OH)$ spread factors of $f \lesssim 3.5$ (Nazari *et al.* 2022; Chen *et al.* 2023). There are likely two reasons behind this large scatter for SO_2: one related to both CH_3OH and SO_2 ice environments, and another related to post-desorption processing of SO_2.

Compared to methanol, the body of knowledge on interstellar SO_2 formation in cold environments is still somewhat scarce. Currently, its main proposed formation routes generally involve SO and a source of oxygen as reactants (Hartquist *et al.* 1980; Charnley 1997; Atkinson *et al.* 2004; Blitz *et al.* 2000; Woods *et al.* 2015; Vidal & Wakelam 2018; Laas & Caselli 2019):

$$SO + OH \rightarrow SO_2 + H \tag{8.6}$$

$$SO + O_2 \rightarrow SO_2 + O \tag{8.7}$$

$$SO + O \rightarrow SO_2. \tag{8.8}$$

In the gas phase, such routes are usually not viable at temperatures below 100 K (e.g., van Gelder *et al.* 2021). One exception might be Reaction 8.6, for which rate constants have been predicted to range from $\sim(2-3)\times10^{-10}$ cm^3 s^{-1} for temperatures between 10 and 100 K (Fuente *et al.* 2019). Still, observed gaseous abundances of SO_2 in both diffuse and dense

clouds are $\sim 10^{-6}$–10^{-5} with respect to CO (Turner 1995; Cernicharo *et al.* 2011, see also Table 4 in Laas & Caselli 2019), which are three to four orders of magnitude lower than ice abundances. Adsorption of SO_2 from the gas phase therefore cannot account for the ice observations. Rather, solid-phase routes to SO_2 must be considered, for which Reactions 8.6−8.8 are also good candidates (Smardzewski 1978; Moore *et al.* 2007; Ferrante *et al.* 2008; Chen *et al.* 2015; Vidal *et al.* 2017).

Like SO_2, gas-phase abundances of SO with respect to CO are still orders of magnitude smaller than those of SO_2 in the ices (Turner 1995; Lique *et al.* 2006; Neufeld *et al.* 2015). Thus, even if all SO adsorbed from the gas phase would be converted to SO_2, it would still be insufficient to explain SO_2 abundances. Alternatively, S atoms adsorbed on the ices could react with O or OH to form SO through

$$\mathrm{s{-}S + s{-}O \rightarrow s{-}SO}, \tag{8.9}$$

$$\mathrm{s{-}S + s{-}OH \rightarrow s{-}SO + s{-}H}, \tag{8.10}$$

which in turn can lead to SO_2 ice via Reactions 8.6 − 8.8. Atomic S can also directly form SO_2 ice by reacting with O_2:

$$\mathrm{s{-}S + s{-}O_2 \rightarrow s{-}SO_2}. \tag{8.11}$$

In addition to the atomic form, interactions of HS radicals with O can efficiently produce SO ice:

$$\mathrm{s{-}HS + s{-}O \rightarrow s{-}SO + s{-}H}. \tag{8.12}$$

Most of these routes have been probed in the laboratory by a number of experimental works involving H_2S ices mixed with oxygen-bearing molecules (e.g., CO_2 or H_2O) and exposed to energetic processing (such as UV photons or protons) to generate the open-shell species (Smardzewski 1978; Moore *et al.* 2007; Ferrante *et al.* 2008; Chen *et al.* 2015). Indeed, HS radicals are thought to be formed in ices via both the hydrogenation of adsorbed S atoms and the destruction of H_2S molecules. The latter can occur either through energetic processing, as mentioned above, or due to H-induced abstraction reactions (Oba *et al.* 2018, 2019; Santos *et al.* 2023b). Furthermore, Laas & Caselli (2019) assert that Reactions 8.7 and 8.8 are hindered in ices due to the high diffusion and binding energies of the reactants. Radical and atom formation through energetic processing could partially circumvent this issue.

Irrespective of the mechanism to originate SO_2, all routes require an oxygen-rich environment to take place. Such an environment is more likely to occur in the earlier phases of the pre-stellar stage, during which H_2O ices grow from the hydrogenation of O, O_2, and O_3 (e.g., Tielens & Hagen 1982; Miyauchi *et al.* 2008; Ioppolo *et al.* 2008; Lamberts *et al.* 2016). Therefore, SO_2 should be formed simultaneously with H_2O during the low-density stage of pre-stellar cores. In contrast, CH_3OH is mainly formed at a much later stage, when densities are high enough for CO to catastrophically freeze-out onto the grains ($A_v > 9$, $n_H \gtrsim 10^5$ cm^{-3}). This discrepancy in the formation timeline of the two species means that they will be subject to different physical conditions and collapse timescales, which may explain the large scatter in the observed ratios. While it is true that ice observations of SO_2 have so far been best described by laboratory measurements of SO_2 in a CH_3OH-rich environment (Boogert *et al.* 1997; Rocha *et al.* 2024), the SO_2 ice feature at 7.6 μm was shown to be highly sensitive to ice mixtures and temperatures (Boogert *et al.* 1997). Hence, further systematic infrared characterizations of SO_2, perhaps with a combination of tertiary ice mixtures including H_2O, would be beneficial to better constrain the chemical environment of this molecule.

A complementary explanation for the scatter in $N(SO_2)/N(CH_3OH)$ is the reprocessing of SO_2 in the gas phase. The SO_2 emission probed in this work traces the hot core region surrounding the protostar, where thermal heating has led the volatile ice content to fully sublimate. At the typically warmer temperatures of such environments ($\gtrsim$100 K), the conditions

become favorable for Reactions 8.6−8.8 to take place in the gas phase (Hartquist *et al.* 1980; van Gelder *et al.* 2021). Given the large variation of source structures and physical conditions associated with massive protostars, the degree to which such reactions occur will likely vary considerably from source to source and are thus expected to result in a wide scatter of SO_2 column densities. Indeed, the models in Vidal & Wakelam (2018) predict that the gaseous SO_2 abundances in protostars are particularly subject to large variations depending on the composition of the parent cloud and the temperature. Furthermore, van Gelder *et al.* (2021) show that gas-phase SO_2 formation is strongly linked to the local UV radiation field since the strength of the latter will largely affect the distribution of reactants. These properties are expected to vary considerably from one massive source to another.

In addition to SO_2, CH_3OH ices typically show considerable variations in column density from source to source (Öberg *et al.* 2011a), which could be contributing to the scatter seen for $N(SO_2)/N(CH_3OH)$. Nonetheless, the larger spread for $N(SO_2)$ compared to other species relative to $N(CH_3OH)$ (e.g., Nazari *et al.* 2022; Chen *et al.* 2023 and the $N(OCS)/N(CH_3OH)$ ratios in this work) points to a significant effect directly associated with SO_2. Differences in the emitting area of SO_2 and CH_3OH could also play a part in the scatter (Nazari *et al.* 2024), albeit to a lesser extent since experimental laboratory sublimation temperatures of SO_2 and CH_3OH are generally quite similar (at ∼120 K and ∼145 K, respectively; Kaňuchová *et al.* 2017; Mifsud *et al.* 2023; Carrascosa *et al.* 2023). Co-desorption with H_2O can potentially raise the sublimation temperature of SO_2, but not enough to result in an appreciable difference to CH_3OH (see, e.g., Fraser *et al.* 2001 for sublimation temperatures of H_2O). Overall, both the origin of SO_2 in ices and its fate after sublimation are likely to play a part in the large scatter seen in Fig. 8.6.

In dark clouds, the ice ratios of $N(SO_2)/N(CH_3OH)$ are generally lower than in the protostellar phase (both for ice and gas observations) by about one order of magnitude. This discrepancy could indicate some additional production of SO_2 during the protostellar phase, conceivably due to the enhanced UV radiation field produced in such environments. Cometary ratios are marginally higher, but still in a reasonably good agreement with protostellar ices, and are larger than the weighted median for gas-phase MYSOs by a factor of ~ 6. As for the case of OCS, causes for this enhancement could be additional processing of SO_2 during the protostellar disk phase, or as a result of selective CH_3OH destruction before incorporation into comets. Given that SO_2 and CH_3OH are proposed to inhabit different ice phases, this supposition is not a priori unreasonable. In summary, the ratios shown in Fig. 8.6 support the hypothesis of a moderate, but not complete inheritance of SO_2 ices from the pre-stellar phase into comets.

8.4.3 SO_2 versus OCS

The column density ratios for SO_2/OCS as a function of luminosity agree with the conclusions drawn in the previous subsections (see Appendix 8.7.10). Figure 8.7 presents the distribution histograms of $N(SO_2)$ and $N(OCS)$ with respect to $N(CH_3OH)$ derived in this work. Each $N(X)/N(CH_3OH)$ is normalized to its own weighted median, so that both distributions are centered on 1 (i.e., 0 in log space). This figure clearly shows the distinctive behaviors of SO_2 and OCS, emphasizing that the latter is likely much more strongly linked to CH_3OH than the former. Furthermore, it suggests that the reprocessing of SO_2 upon desorption is much more drastic than for OCS, in agreement with the models in Vidal & Wakelam (2018).

Another relevant source of information is to compare the direct correlation between SO_2 and OCS abundances with respect to CH_3OH (Fig. 8.8). Based on the derived Pearson coefficient ($r = 0.32$), a weak correlation appears to exist between $N(SO_2)/N(CH_3OH)$ and $N(OCS)/N(CH_3OH)$. This is supported by the Spearman's correlation test, which yields a coefficient of $\rho = 0.38$ with a p-value of 0.05. The fact that this association is weak is unsurprising, since the bulk of SO_2 and OCS probably originate from two different ice environments, which means that their chemistry cannot be strongly linked. Nonetheless,

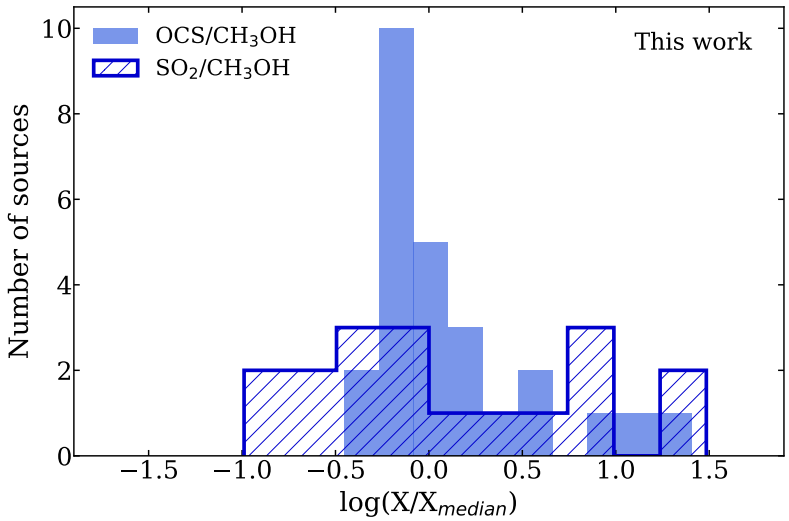

Figure 8.7: Same as Fig. 8.5, but for $N(SO_2)/N(CH_3OH)$ (hatched) and $N(OCS)/N(CH_3OH)$ (filled) gas-phase observations from the ALMAGAL dataset. In this case, each ratio is normalized to its own weighted median value.

some modest connection seems to be present between the two sulfur-bearing species. This could be due, for instance, to one species providing a source of sulfur that is converted into the other. Indeed, SO_2 ices can be dissociated into S atoms upon energetic processing, which could in turn react with CO to form OCS. Likewise, OCS molecules can also yield S atoms upon fragmentation, which in turn can react with H_2O to form SO_2 (Ferrante *et al.* 2008). Alternatively, this correlation could be the result of a common precursor to both species, such as atomic S or SH radicals. We emphasize, however, that the correlation is weak and reliant on the high-abundance end of the range of values, and thus should be considered with caution.

8.5 Conclusions

In this work we analyzed the emission of OCS and SO_2 toward 26 line-rich MYSOs observed as part of the ALMAGAL survey. We compared their abundances with respect to methanol with other gas-phase observations toward low-mass sources, as well as in interstellar ices and comets. Our main findings are as follows:

- The gaseous column density ratios of OCS/CH_3OH and SO_2/CH_3OH show no trend with respect to luminosity, pointing to an early onset formation of both sulfur-bearing molecules before star formation begins. The ratios in protostellar ices are consistent with the weighted medians of the ALMAGAL dataset, suggesting an icy origin for both OCS and SO_2 followed by thermal sublimation upon heating from the protostar.
- A large scatter in relative abundances is observed with ALMAGAL for gaseous SO_2/CH_3OH ($f = 5.8$), but not for OCS/CH_3OH ($f = 2.8$). We suggest that this is due to different chemical environments during the formation of SO_2 and OCS, with the former being formed during the low-density phase of cold clouds, and the latter's formation mostly taking place during the later, high-density pre-stellar stage. OCS and CH_3OH both originate from reactions with CO ice. Post-desorption processing likely

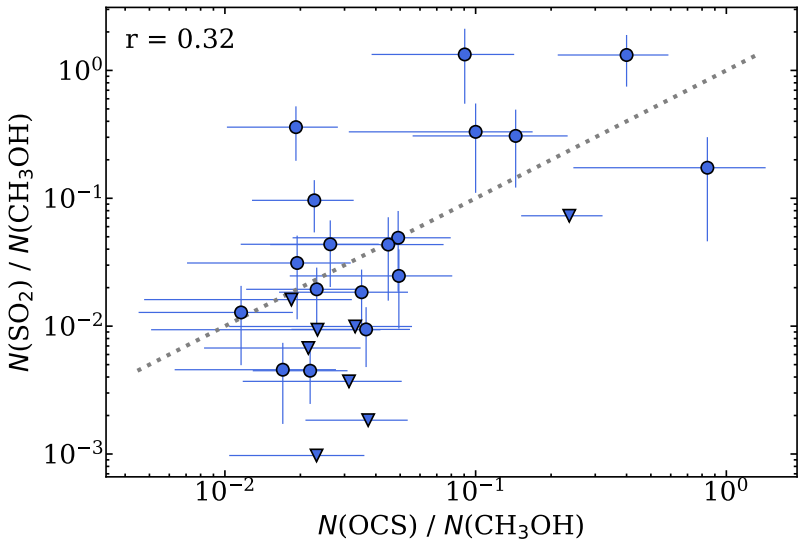

Figure 8.8: Relative abundances $N(SO_2)/N(CH_3OH)$ versus $N(OCS)/N(CH_3OH)$ for the ALMAGAL dataset analyzed in this work. Upper limits in the $N(SO_2)/N(CH_3OH)$ ratios are denoted by downward facing triangles. The Pearson correlation coefficient (excluding upper limits) is shown in the upper-left corner, and the dotted line traces the 1:1 relation.

also contributes to the spread in $N(SO_2)/N(CH_3OH)$.

- For OCS, dark cloud ice values are in remarkably good agreement with both protostellar ice and gas observations. Cometary ratios are also quite similar, at only a factor of ∼4 higher. Some extra formation of OCS during the protostellar disk phase has been suggested as a root for this difference, as well as selective destruction of CH_3OH. Nonetheless, all ratios point to a significant inheritance of OCS ices throughout the different stages of star formation.
- The gaseous abundances of SO_2 relative to CH_3OH derived in this work agree with both dark-cloud and cometary ice ratios. Values in comets are generally slightly higher (by a factor of ∼6) than in protostars, which in turn are higher than in dark clouds. This could indicate some additional formation of SO_2 during the protostellar and protoplanetary-disk phases, although selective destruction of CH_3OH could also explain such observations in the latter case.
- A weak correlation ($r = 0.32$) is found between $N(SO_2)/N(CH_3OH)$ and $N(OCS)/N(CH_3OH)$. While the bulk of these ices is likely formed in different environments on two distinct evolutionary timescales, some interconversion between SO_2 and OCS is possible and could lead to a weak association. This could also result from a common precursor of the two species, arguably S or HS.

Overall, our findings suggest that OCS and SO_2 differ significantly in both their formation and destruction pathways, but could still potentially share a common history. It should be noted that the dataset studied here is biased in favor of line-rich sources and therefore our results might not represent all massive protostars. Furthermore, it is clear that more observational constraints on interstellar ice column densities of sulfur-bearing species, and in particular of SO_2, are paramount to building a more complete understanding of the origin

and fate of sulfur. The JWST offers a unique opportunity for such constraints to be explored in depth.

8.6 Acknowledgments

Astrochemistry at Leiden is supported by funding from the European Research Council (ERC) under the European Union's Horizon 2020 research and innovation programme (grant agreement No. 101019751 MOLDISK) and the Danish National Research Foundation through the Center of Excellence "InterCat" (Grant agreement no.: DNRF150).

8.7 Appendix

8.7.1 Example of an excluded source

Figure 8.9 contains an example of a source that was excluded from the analysis because of large divergences in the spectral properties between $^{34}SO_2$ and $O^{13}CS$, in this case potentially due to self absorption of the $^{34}SO_2$ lines.

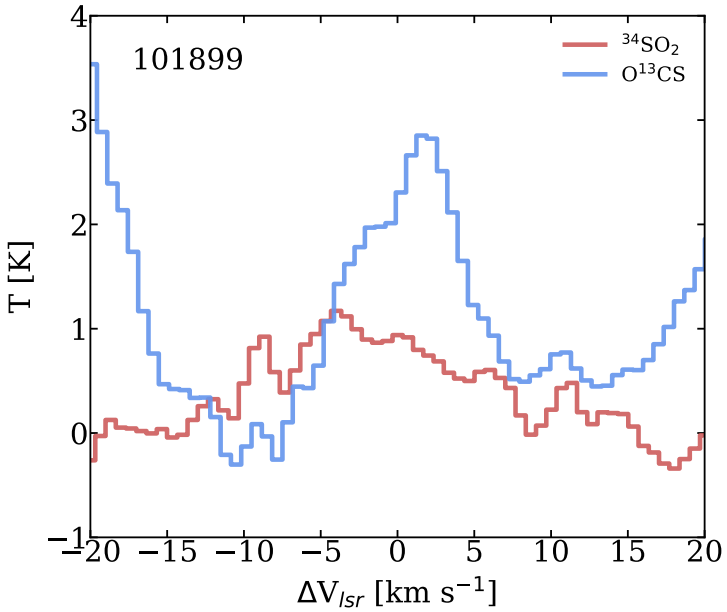

Figure 8.9: Superimposed lines of $^{34}SO_2$ (red) and $O^{13}CS$ (blue) observed toward 101899.

8.7.2 Source properties and observational parameters

The observational parameters for each source and their physical properties are listed in Table 8.2.

Table 8.2: Observational parameters and physical properties of the sources.

Source	R.A. (J2000) [a] (hh:mm:ss.s)	Dec. (J2000) [a] (dd:mm:ss.s)	Beam ($''$)	Line rms [b] (K)	d [c] (kpc)	D_{GC} [d] (kpc)	L_{bol} [e] ($L_\odot$)
126348	18:42:51.98	-03:59:54.37	1.26 × 1.08	0.16	4.41	4.67	6798
615590	09:24:41.96	-52:02:08.04	0.68 × 0.59	0.50	2.70	8.31	5470
644284A	10:31:29.78	-58:02:19.27	0.96 × 0.80	0.32	4.75	8.20	–
693050	12:35:35.05	-63:02:31.19	1.03 × 0.94	0.19	4.31	6.89	12200
705768	13:12:36.17	-62:33:34.43	0.93 × 0.81	0.24	6.88	6.93	91728
707948	13:16:43.19	-62:58:32.83	0.94 × 0.80	0.26	7.14	6.97	196800
717461A	13:43:01.68	-62:08:51.42	1.34 × 1.21	0.22	4.29	6.31	3323
721992	13:51:58.27	-61:15:41.04	0.90 × 0.79	0.37	5.38	6.16	2630
724566	13:59:30.92	-61:48:38.27	0.87 × 0.78	0.34	4.93	6.10	226
732038	14:13:15.05	-61:16:53.19	0.87 × 0.78	0.40	5.64	5.93	74930
744757A	14:45:26.35	-59:49:15.55	1.31 × 1.27	0.15	2.51	6.45	12381
767784	15:29:19.31	-56:31:22.02	1.31 × 1.24	0.16	4.04	5.37	139400
865468A	17:05:10.90	-41:29:06.99	1.32 × 1.14	0.22	3.04	5.17	47824
876288	17:11:51.02	-39:09:29.18	0.92 × 0.69	0.29	5.95	2.58	58410
881427C	17:20:06.12	-38:57:15.84	1.31 × 1.13	0.56	1.50	6.59	458
G023.3891p00.1851	18:33:14.32	-08:23:57.82	1.43 × 1.07	0.18	10.86	4.72	91560
G025.6498p01.0491	18:34:20.92	-05:59:42.08	1.24 × 1.07	0.15	12.20	6.05	424000
G305.2017p00.2072A1	13:11:10.45	-62:34:38.60	1.38 × 1.21	0.21	4.00	6.61	20301
G314.3197p00.1125	14:26:26.25	-60:38:31.26	1.36 × 1.23	0.21	8.25	6.33	66440
G316.6412-00.0867	14:44:18.35	-59:55:11.28	1.32 × 1.25	0.15	2.73	6.35	8080
G318.0489p00.0854B	14:53:42.64	-59:08:53.02	1.31 × 1.27	0.15	3.18	6.07	36480
G318.9480-00.1969A1	15:00:55.28	-58:58:52.60	1.30 × 1.27	0.15	10.40	6.83	209000
G323.7399-00.2617B2	15:31:45.45	-56:30:49.84	1.29 × 1.25	0.15	3.20	5.79	1529
G327.1192p00.5103	15:47:32.72	-53:52:38.60	0.90 × 0.72	0.34	4.74	4.81	54270
G343.1261-00.0623	16:58:17.22	-42:52:07.54	1.33 × 1.15	0.21	2.00	6.16	33800
G345.5043p00.3480	17:04:22.89	-40:44:23.06	1.34 × 1.15	0.20	2.00	6.13	29498

[a] The coordinates correspond to the pixel from which the spectra were extracted.
[b] Line rms as computed by Nazari *et al.* (2022).
[c] Distance to the source (Lumsden *et al.* 2013; Mège *et al.* 2021). Typical uncertainties are of ∼0.5 kpc.
[d] Distance to the galactic center assuming the Sun's D_{GC} as 8.05 kpc (Honma *et al.* 2015).
[e] Bolometric luminosities corrected to the distances d (Lumsden *et al.* 2013; Elia *et al.* 2017). For regions with multiple cores, the fraction of each individual source was estimated by dividing the total luminosity over all the cores weighted by their peak continuum flux (see also van Gelder *et al.* 2022b and Nazari *et al.* 2022). No estimations for 644284A are available, so a generic $L_{bol} \sim 10^4$ $L_\odot$ is assumed.

8.7.3 List of transitions

Table 8.7.3 lists all the transitions of $^{34}SO_2$, $^{33}SO_2$, and $O^{13}CS$ with $E_{up} < 800$ K and $A_{ij} > 10^{-6}$ s^{-1} covered in the data.

Table 8.3: Covered transitions.

Species	Transition	Frequency (MHz)	E_{up} (K)	A_{ij} (s^{-1})
$^{34}SO_2$	26 8 18 − 27 7 21	217412.915	473.565	2.09×10^{-5}
$^{34}SO_2$	31 9 23 − 32 8 24	217902.353	646.797	2.17×10^{-5}
$^{34}SO_2$	11 1 11 − 10 0 10 ⋆	219355.009	60.075	1.11×10^{-4}
$^{34}SO_2$	36 5 31 − 35 6 30	220451.866	675.942	2.61×10^{-5}
$^{33}SO_2$	6 4 2 4.5 − 7 3 5 5.5	217628.227	57.861	1.07×10^{-5}
$^{33}SO_2$	6 4 2 7.5 − 7 3 5 8.5	217628.440	57.861	1.04×10^{-5}
$^{33}SO_2$	6 4 2 5.5 − 7 3 5 6.5	217628.749	57.861	1.03×10^{-5}
$^{33}SO_2$	6 4 2 6.5 − 7 3 5 7.5	217628.884	57.861	1.03×10^{-5}
$^{33}SO_2$	11 1 11 9.5 − 10 0 10 9.5 ⋆	220613.365	60.215	1.60×10^{-6}
$^{33}SO_2$	11 1 11 9.5 − 10 0 10 8.5 ⋆	220617.426	60.215	1.11×10^{-4}
$^{33}SO_2$	11 1 11 12.5 − 10 0 10 11.5 ⋆	220617.778	60.215	1.12×10^{-4}
$^{33}SO_2$	11 1 11 10.5 − 10 0 10 10.5 ⋆	220619.743	60.215	1.93×10^{-6}
$^{33}SO_2$	11 1 11 10.5 − 10 0 10 9.5 ⋆	220620.374	60.215	1.10×10^{-4}
$^{33}SO_2$	11 1 11 11.5 − 10 0 10 10.5 ⋆	220620.716	60.215	1.11×10^{-4}
$^{33}SO_2$	11 1 11 11.5 − 10 0 10 11.5 ⋆	220624.670	60.215	1.33×10^{-6}
$O^{13}CS$	18 − 17 ⋆	218198.998	99.49	3.01×10^{-5}

⋆ Detected transitions.

8.7.4 Best-fit models for all sources

Figures 8.10 and 8.11 show the best-fit models derived by the grid-fitting approach for each source in the ALMAGAL subset analyzed here. The former contains the results for $^{34}SO_2$, and the latter for $O^{13}CS$.

8.7.5 Integrated intensity map of 693050

Figure 8.12 shows the integrated intensity maps of source 693050 for $^{34}SO_2$ $11_{1,11}$–$10_{0,10}$ and $O^{13}CS$ 18−17. The offset in the emission to the continuum peak is likely due to effects of optically thick dust at these wavelengths.

8.7.6 Best-fit parameters of $^{34}SO_2$ and $O^{13}CS$

Tables 8.4 and 8.5 list the best-fit parameters for $^{34}SO_2$ and $O^{13}CS$, respectively, obtained with the grid fitting approach toward all sources. The isotope ratios for each source and corresponding estimated column densities of the main isotopologs are also reported.

Table 8.4: Fitting results for $^{34}SO_2$.

Source	$^{34}SO_2$			($^{32}S/^{34}S$) [c]	SO_2
	N [a] (cm^{-2})	FWHM [b] ($km\ s^{-1}$)	V_{lsr} [b] ($km\ s^{-1}$)		N [d] (cm^{-2})
126348	$<4.5\times10^{14}$	[7.5]	76.9	20	$<8.8\times10^{15}$
615590	$(4.0\pm0.8)\times10^{16}$	4.3±0.4	40.5	23	$(9.0\pm2.4)\times10^{17}$
644284A	$(2.5\pm0.5)\times10^{16}$	7.4±0.5	2.60	22	$(5.6\pm1.5)\times10^{17}$
693050	$(2.0\pm0.4)\times10^{16}$	5.7±1.6	-41.2	22	$(4.3\pm1.1)\times10^{17}$
705768	$<6.0\times10^{14}$	[6.7]	-34.1	22	$<1.3\times10^{16}$
707948	$(2.5\pm0.7)\times10^{16}$	8.5±2.5	-32.6	22	$(5.4\pm1.6)\times10^{17}$
717461A	$(5.0\pm1.0)\times10^{15}$	5.7±0.5	-51.3	21	$(1.1\pm0.3)\times10^{17}$
721992	$(1.3\pm0.3)\times10^{15}$	3.2±0.7	-57.3	21	$(2.6\pm0.8)\times10^{16}$
724566	$<7.0\times10^{14}$	[6.0]	-57.3	21	$<1.5\times10^{16}$
732038	$(4.0\pm0.8)\times10^{15}$	5.2±0.6	-62.5	21	$(8.3\pm2.0)\times10^{16}$
744757A	$(2.5\pm0.5)\times10^{15}$	6.2±0.7	-40.5	21	$(5.3\pm1.3)\times10^{16}$
767784	$(1.6\pm0.3)\times10^{15}$	4.1±0.3	-67.9	20	$(3.2\pm0.8)\times10^{16}$
865468A	$<6.0\times10^{14}$	[8.0]	-27.3	20	$<1.2\times10^{16}$
876288	$<5.0\times10^{14}$	4.8±0.5	-96.2	18	$<9.2\times10^{15}$
881427C	$<1.1\times10^{15}$	[5.5]	-10.4	18	$<2.0\times10^{16}$
G023.3891p00.1851	$<2.5\times10^{14}$	[4.0]	75.5	21	$<5.3\times10^{15}$
G025.6498p01.0491	$(3.2\pm0.6)\times10^{15}$	6.2±0.9	42.4	21	$(6.6\pm1.6)\times10^{16}$
G305.2017p00.2072A1	$(1.0\pm0.2)\times10^{15}$	4.2±0.5	-40.9	21	$(2.1\pm0.5)\times10^{16}$
G314.3197p00.1125	$<3.8\times10^{14}$	5.0±0.5	-49.0	21	$<8.0\times10^{15}$
G316.6412-00.0867	$(1.6\pm0.3)\times10^{15}$	8.2±0.5	-20.5	21	$(3.3\pm0.8)\times10^{16}$
G318.0489p00.0854B	$(4.0\pm0.8)\times10^{15}$	6.6±0.4	-50.6	21	$(8.3\pm2.1)\times10^{16}$
G318.9480-00.1969A1	$(2.0\pm0.5)\times10^{15}$	7.0±4.0	-33.5	22	$(4.3\pm1.3)\times10^{16}$
G323.7399-00.2617B2	$(1.3\pm0.3)\times10^{15}$	6.6±0.5	-51.4	21	$(2.6\pm0.6)\times10^{16}$
G327.1192p00.5103	$(6.3\pm1.3)\times10^{15}$	6.0±0.7	-83.2	20	$(1.3\pm0.3)\times10^{17}$
G343.1261-00.0623	$(3.2\pm0.6)\times10^{15}$	7.3±0.5	-31.5	21	$(6.6\pm1.6)\times10^{17}$
G345.5043p00.3480	$(5.0\pm1.0)\times10^{15}$	7.9±0.6	-17.5	21	$(1.1\pm0.3)\times10^{17}$

[a] Column densities are calculated using the grid fitting method. 3σ upper limits are derived by manual fitting.

[b] Square brackets denote FWHM values kept fixed during the fitting. For the sources where no $^{34}SO_2$ emission is detected, their FWHM and V_{lsr} are fixed to the values reported for $CH_3{}^{13}CN$ toward the same source (Nazari *et al.* 2022). For the rest of the sources the velocities are fixed to the best-fitted values derived by the manual approach.

[c] Values are rounded to zero decimals.

[d] Column densities of the main isotopologs are derived from the fitting results of the rare isotopologs and considering the isotope ratios.

Table 8.5: Fitting results for $O^{13}CS$.

Source	$O^{13}CS$			($^{12}C/^{13}C$)	OCS
	N (cm^{-2})	FWHM (km s^{-1})	V_{lsr} (km s^{-1})		N (cm^{-2})
126348	$(5.0\pm1.3)\times10^{14}$	8.7±2.3	75.1	43	$(2.2\pm0.6)\times10^{16}$
615590	$(7.9\pm2.1)\times10^{14}$	3.8±1.6	40.0	60	$(4.8\pm1.4)\times10^{16}$
644284A	$(6.3\pm1.3)\times10^{14}$	6.2±1.7	1.50	60	$(3.8\pm0.9)\times10^{16}$
693050	$(2.5\pm0.7)\times10^{15}$	4.8±0.5	-41.4	54	$(1.3\pm0.4)\times10^{17}$
705768	$(7.9\pm2.1)\times10^{14}$	4.4±0.9	-34.1	54	$(4.3\pm1.3)\times10^{16}$
707948	$(1.0\pm0.3)\times10^{16}$	11.0±2.0	-31.3	54	$(5.4\pm1.6)\times10^{17}$
717461A	$(5.0\pm1.0)\times10^{14}$	4.4±0.9	-51.5	51	$(2.5\pm0.6)\times10^{16}$
721992	$(2.5\pm0.5)\times10^{15}$	3.0±0.1	-57.9	50	$(1.3\pm0.3)\times10^{17}$
724566	$(2.5\pm0.5)\times10^{15}$	4.6±0.6	-56.4	50	$(1.3\pm0.3)\times10^{17}$
732038	$(7.9\pm1.6)\times10^{14}$	4.3±1.2	-63.8	49	$(3.9\pm1.0)\times10^{16}$
744757A	$(6.3\pm1.3)\times10^{14}$	5.1±1.2	-41.0	52	$(3.3\pm0.8)\times10^{16}$
767784	$(6.3\pm1.3)\times10^{14}$	4.0±0.7	-67.2	46	$(2.9\pm0.7)\times10^{16}$
865468A	$(6.3\pm1.3)\times10^{15}$	5.8±0.5	-26.8	45	$(2.9\pm0.7)\times10^{17}$
876288	$(3.2\pm0.8)\times10^{14}$	3.0±0.6	-96.5	33	$(1.1\pm0.3)\times10^{16}$
881427C	$(7.9\pm1.6)\times10^{15}$	5.3±0.4	-11.3	52	$(4.1\pm1.0)\times10^{17}$
G023.3891p00.1851	$(4.0\pm0.8)\times10^{14}$	3.0±0.1	75.6	43	$(1.7\pm0.5)\times10^{16}$
G025.6498p01.0491	$(1.6\pm0.3)\times10^{15}$	6.0±0.9	41.3	50	$(7.9\pm1.9)\times10^{16}$
G305.2017p00.2072A1	$(7.9\pm2.1)\times10^{14}$	3.5±1.0	-41.7	52	$(4.2\pm1.2)\times10^{16}$
G314.3197p00.1125	$(5.0\pm1.0)\times10^{14}$	5.9±0.8	-49.8	51	$(2.6\pm0.6)\times10^{16}$
G316.6412-00.0867	$(2.5\pm0.5)\times10^{15}$	5.5±0.4	-19.4	51	$(1.3\pm0.3)\times10^{17}$
G318.0489p00.0854B	$(1.0\pm0.3)\times10^{15}$	5.7±1.1	-50.9	50	$(5.0\pm1.5)\times10^{16}$
G318.9480-00.1969A1	$(4.0\pm0.8)\times10^{15}$	4.7±0.3	-34.5	53	$(2.1\pm0.5)\times10^{17}$
G323.7399-00.2617B2	$(2.0\pm0.4)\times10^{15}$	3.9±0.5	-52.1	48	$(9.7\pm2.4)\times10^{16}$
G327.1192p00.5103	$(2.5\pm0.5)\times10^{15}$	6.7±1.7	-84.1	44	$(1.1\pm0.3)\times10^{17}$
G343.1261-00.0623	$(2.5\pm0.7)\times10^{15}$	8.9±2.1	-32.5	50	$(1.3\pm0.4)\times10^{17}$
G345.5043p00.3480	$(4.0\pm1.0)\times10^{15}$	6.9±1.9	-17.5	50	$(2.0\pm0.6)\times10^{17}$

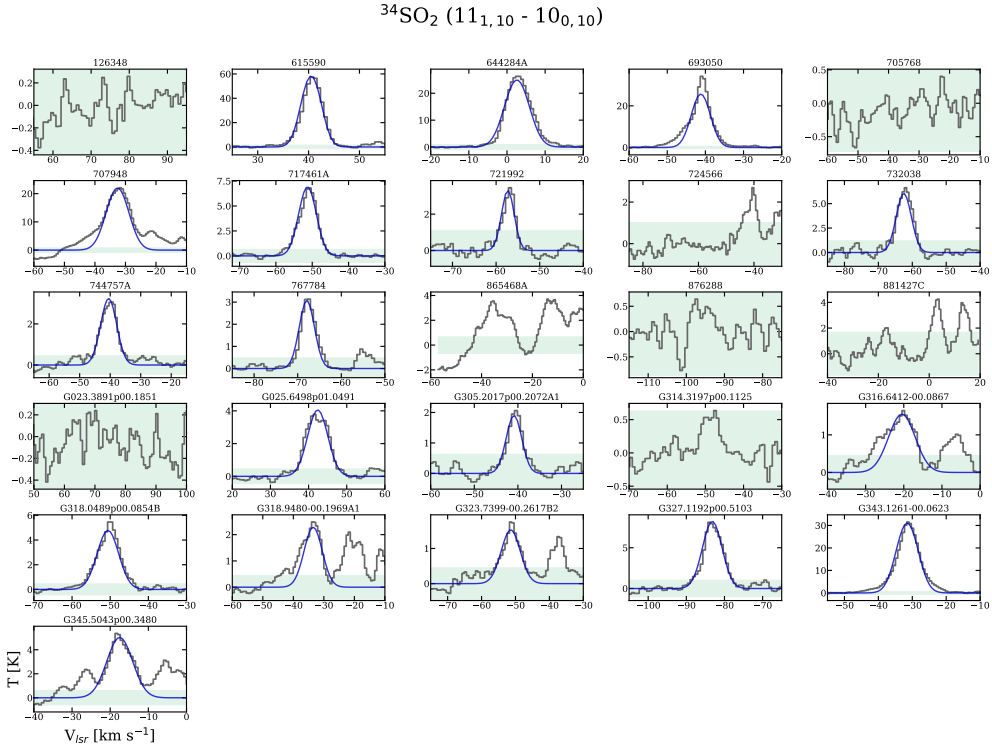

Figure 8.10: Observed spectra toward each source (gray) superimposed by its best-fit model for $^{34}SO_2$ (blue). The green shadowed area delimits the 3σ threshold. The name of each source is shown on the top of each panel.

8.7.7 FWHM and V_{lsr} of $^{34}SO_2$ and $O^{13}CS$ compared to CH_3OH

Figure 8.13 shows the ratios of FWHM and differences of V_{lsr} for $^{34}SO_2$ and $O^{13}CS$ with respect to CH_3OH.

8.7.8 Best-fit parameters of $^{33}SO_2$

Table 8.6 lists the best-fit parameters for the $^{33}SO_2$ transitions in the sources where it could be constrained.

8.7.9 Literature ratios

Table 8.7 lists the literature values for $N(SO_2)/N(CH_3OH)$, $N(OCS)/N(CH_3OH)$, and $N(SO_2)/N(OCS)$ gathered in this work.

8.7.10 $N(SO_2)/N(OCS)$

The ratios of the derived column densities for SO_2 and OCS are shown in Fig. 8.14 as a function of luminosity. For comparison, ratios measured in the gas phase of low-mass sources are also shown, together with ice observations toward comets, dark clouds, as well as both low- and high-mass protostars.

Table 8.6: Fitted parameters for $^{33}SO_2$.

Source	$^{33}SO_2$			($^{32}S/^{33}S$) [b]	SO_2 from $^{33}SO_2$	SO_2 from $^{34}SO_2$
	N (cm^{-2})	FWHM [a] (km s^{-1})	V_{lsr} [a] (km s^{-1})		N (cm^{-2})	N (cm^{-2})
615590	$(1.0\pm0.2)\times10^{16}$	3.7	40.5	93	$(9.3\pm0.9)\times10^{17}$	$(9.0\pm2.4)\times10^{17}$
644284A	$(7.0\pm1.0)\times10^{15}$	6.0	2.6	92	$(6.5\pm1.4)\times10^{17}$	$(5.6\pm1.5)\times10^{17}$
693050	$(6.0\pm1.5)\times10^{15}$	3.5	-41.2	89	$(5.3\pm0.5)\times10^{17}$	$(4.3\pm1.1)\times10^{17}$
G343.1261-00.0623	$(9.5\pm1.5)\times10^{15}$	7.3	-31.5	87	$(8.3\pm1.8)\times10^{17}$	$(6.6\pm1.6)\times10^{17}$

[a] Uncertainties in the FWHMs and V_{lsr} are $\lesssim 0.5$ km s^{-1}.
[b] Values are rounded to zero decimals.

Table 8.7: References of literature ratios.

Object	$N(SO_2)/N(CH_3OH)$	$N(OCS)/N(CH_3OH)$	$N(SO_2)/N(OCS)$
		Gas phase	
MYSOs [a]	(1), (2), (4), (10), (11)	(1), (2), (4), (10), (11)	(1) − (13)
LYSOs [b]	(15), (16), (22), (23)	(15) − (17), (19) − (23)	(14) − (16), (18), (22), (23), (24)
		Interstellar ices	
Dark clouds [c]	(25)	(25)	(25)
MYSOs [d]	(26), (27)	(27)	(26), (27)
LYSOs [e]	(28), (29)		
		Solar System	
Comets [f]	(30), (31), (33), (36), (37)	(30) − (38)	(30), (31), (33), (36), (37)

[a] (1) Hatchell *et al.* (1998); (2) van der Tak *et al.* (2000); (3) Hofner *et al.* (2001); (4) van der Tak *et al.* (2003); (5) Osorio *et al.* (2009); (6) Herpin *et al.* (2009); (7) Cesaroni *et al.* (2010); (8) Pillai *et al.* (2011); (9) van der Tak *et al.* (2013); (10) Gieser *et al.* (2019); (11) Fuente *et al.* (2021); (12) Mininni *et al.* (2021); (13) Fontani *et al.* (2023).

[b] (14) Tafalla *et al.* (2000); (15) Jørgensen *et al.* (2018); (16) Drozdovskaya *et al.* (2018); (17) Sahu *et al.* (2019); (18) Agúndez *et al.* (2019); (19) van Gelder *et al.* (2020); (20) Manigand *et al.* (2020); (21) Yang *et al.* (2020); (22) Artur de la Villarmois *et al.* (2023); (23) Kushwahaa *et al.* (2023); (24) Esplugues *et al.* (2023).

[c] (25) McClure *et al.* (2023).

[d] (26) Boogert *et al.* (1997); (27) Boogert *et al.* (2022).

[e] (28) Tobin *et al.* (2016); (29) Rocha *et al.* (2024).

[f] (30) Dello Russo *et al.* (1998); (31) Bockelée-Morvan *et al.* (2000a); (32) Mumma *et al.* (2011); (33) Le Roy *et al.* (2015); (34) Biver *et al.* (2015); (35) Dello Russo *et al.* (2016); (36) Calmonte *et al.* (2016); (37) Schuhmann *et al.* (2019); (38) Saki *et al.* (2020).

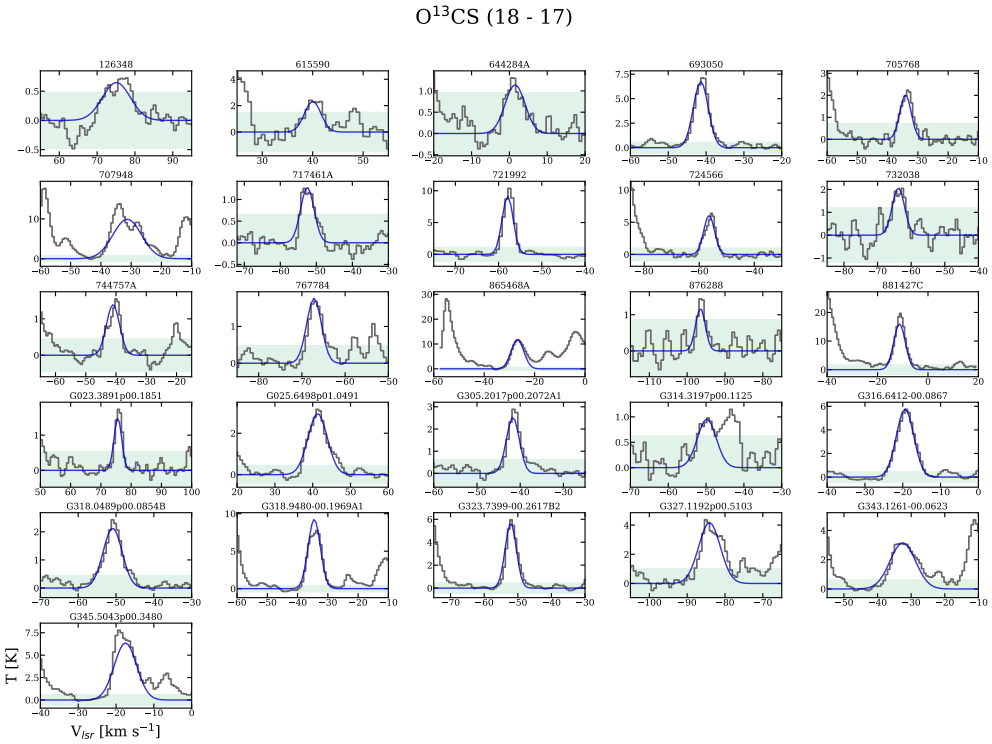

Figure 8.11: Same as Fig. 8.10, but for $O^{13}CS$.

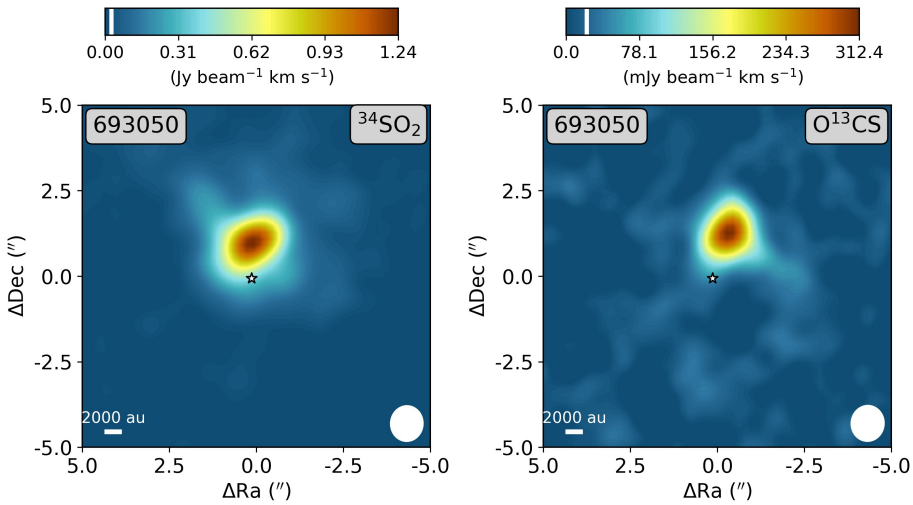

Figure 8.12: Integrated intensity maps of the $^{34}SO_2$ $11_{1,11}$–$10_{0,10}$ (left) and $O^{13}CS$ 18−17 (right) lines for 693050. The integration limits are set to [-5, 5] km s^{-1} with respect to the source's $V_{\rm lsr}$. The white star denotes the source positions derived from the continuum emission, and the 3σ threshold is delimited by the white line in the color bars. The beam size is shown in the lower-right corner of each panel, and a scale bar is depicted in the lower left.

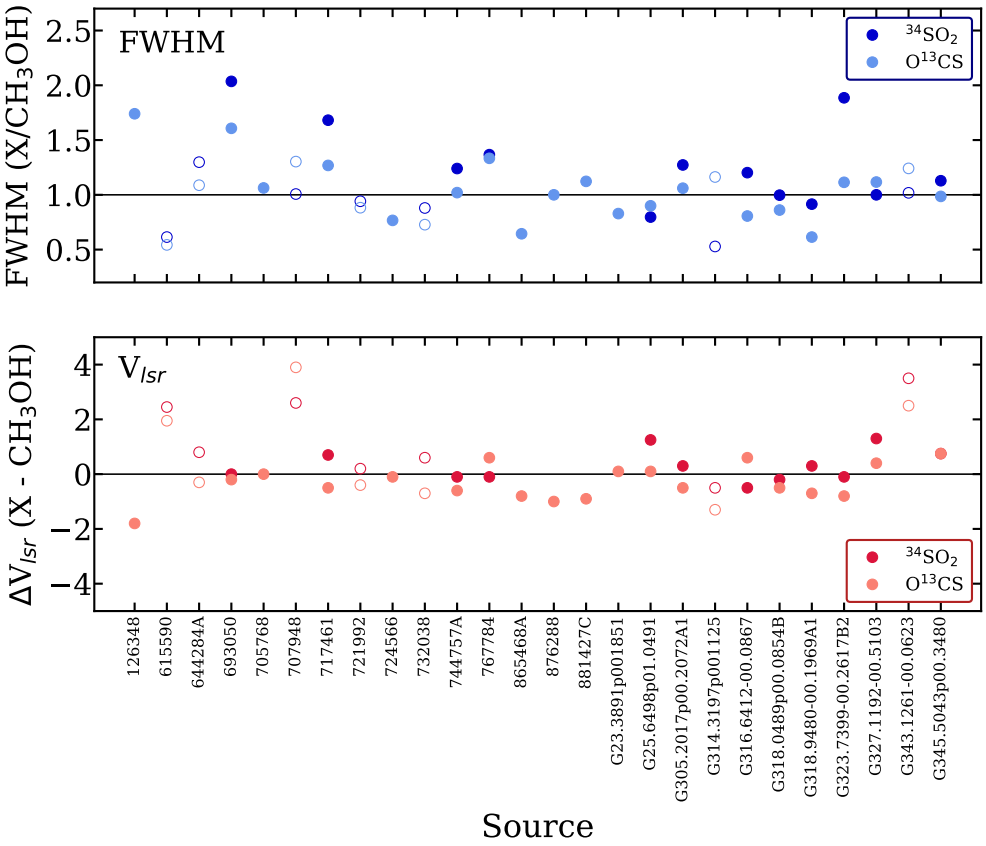

Figure 8.13: FWHM ratios (upper panel) and $V_{\rm lsr}$ differences (lower panel) with respect to $CH_3{}^{18}OH$. For sources in which $CH_3{}^{18}OH$ was not detected by van Gelder *et al.* (2022a), the main CH_3OH isotopolog was used (empty markers). Values for $^{34}SO_2$ are shown in darker colors and for $O^{13}CS$ in lighter colors.

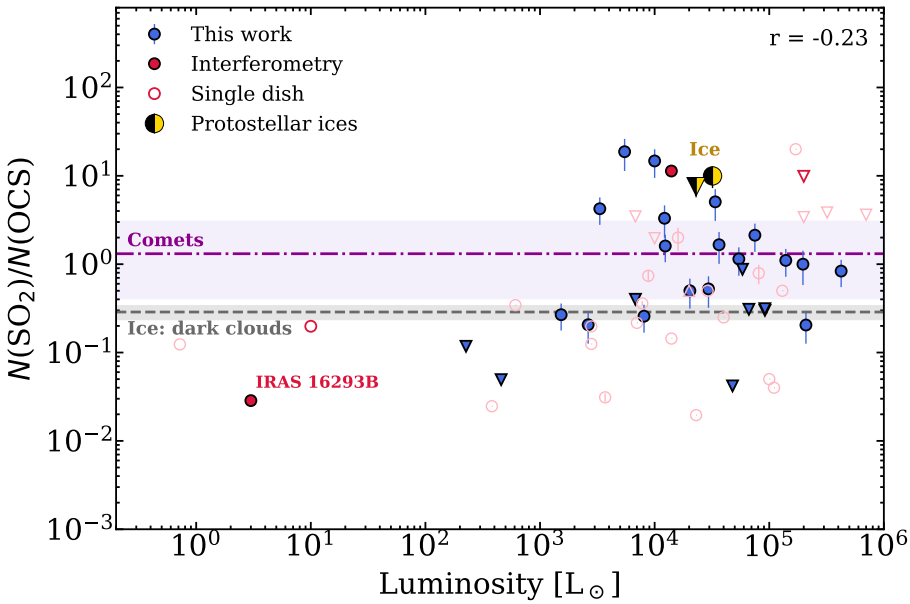

Figure 8.14: Same as Figure 8.4, but for $N(SO_2)/N(OCS)$. Literature ratios with $N(SO_2)$ derived from the main isotopologue are signaled by light red markers to differentiate from values derived from $^{34}SO_2$, which are shown in darker red.